HiSST: 3rd International Conference on
High-Speed Vehicle Science Technology
14 -19 April 2024, Busan, Korea

Influence of the Swing Angle on the Performance of Planar SSSL Nozzle

Rui. Li[1], Jinglei Xu[2], Haiyin Lv[3]

State Key Laboratory of Mechanics and Control of Aeronautics and Astronautics Structures, Nanjing University of Aeronautics and Astronautics, Nanjing, 210016, People's Republic of China

Jiangsu Province Key Laboratory of Aerospace Power System, College of Energy & Power Engineering, Nanjing University of Aeronautics and Astronautics, Nanjing, 210016, People's Republic of China

Abstract

This study numerically investigates the performance of supersonic splitline nozzles concerning interactions between the airflow and the particles of aluminum trioxide. The existence of the initial arc radius concentrates heavy particles along the axis and scatters light particles to the nozzle transition region. The total length influences the shock wave reflections in the nozzle. The convex diverging profile with a large secondary radius is beneficial for balancing performance parameters. In addition, the swing center upstream of the throat can enlarge the lateral force. Based on these recognitions, the nozzle configuration with an initial arc radius of 10 mm, a total nozzle length of 50 mm, a convex secondary arc of 200 mm, and a swing center at the throat is finally selected to obtain the optimal aerodynamic performance. With the increase in the swing angle from 0 to 6°, the thrust coefficient only drops by 1.89% and always keeps above 0.9356. Meanwhile, its amplification factor exceeds 1.302, and its maximum thrust vector angle is 7.796°.

Keywords: *Supersonic split line nozzle, Swing angle, Amplification factor, Gas-particle flow, Shock wave*

Nomenclature

ρ – density
t – time
u – velocity
p – pressure
F – force
σ – viscous stress tensor
e – internal energy per unit mass
J – diffusion term
h – enthalpy per unit mass
T – Temperature

1. Introduction

In order to change the flight direction of the rocket during the ascending stage and the cruise condition and increase agility and manoeuvrability, it is necessary to exert a lateral force on the rocket body timely. Three mature methods can realize this goal based on changing the nozzle flowfields. The first one is the mechanical disturbance that utilizes the intrusive rudder in the exhaust flow to create force vector increment; the second one is the secondary injection on the nozzle wall that induces the shock

[1] *Postdoctor, Nanjing University of Aeronautics and Astronautics, ruili@nuaa.edu.cn*
[2] *Professor, Nanjing University of Aeronautics and Astronautics, xujl@nuaa.edu.cn*
[3] *Phd. student, Nanjing University of Aeronautics and Astronautics, haiyinlv@nuaa.edu.cn*

waves to deflect the flow; the third one is the swing nozzle that rotates the nozzle as a whole or generates the dislocation of the nozzle profile. As illustrated in Fig.1, above the axis is the submerged vectored nozzle, and below the axis is the supersonic splitline nozzle. The two types of nozzles have hollow ball joints, which are, respectively, located at the throat and the diverging section. In contrast with the submerged vectored nozzle, the most prominent feature of the supersonic splitline nozzle is the amplification of the lateral force, which means that the vector angle exceeds the swing angle. Meanwhile, the sealing structures of the supersonic splitline nozzle are much simpler, which is beneficial for reducing the cost and promoting reliability. Figure 2 displays the flowfield of the supersonic split line nozzle with a small deflection of the downstream diverging section. Due to the dislocation of the nozzle profiles upstream and downstream of the splitline, the lower and upper walls form a forward-facing step and a backward-facing step, inducing a shock wave and an expansion fan, respectively.

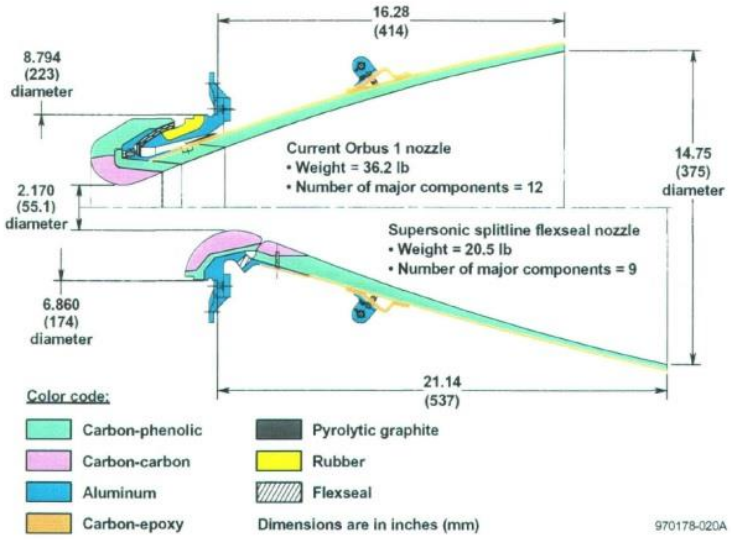

Fig 1. Sectional drawings of the submerged vectored nozzle and supersonic split line nozzle

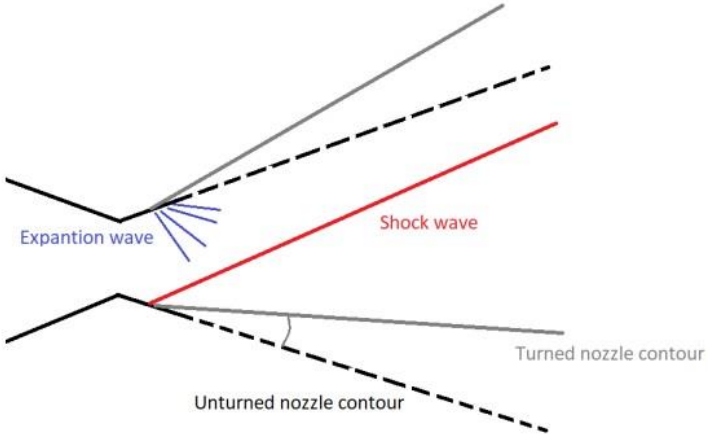

Fig 2. Schematic of the supersonic split line nozzle labelled with expansion and shock waves

Since the 1960s, a series of researches about the supersonic splitline nozzle have been conducted at home and aboard. Strahle [1] adopted a three-dimensional perturbation technique to establish the aerodynamic performance model of the supersonic split line nozzle and made a parametric study of the nozzle size and swing centre. It was observed that the lateral force and the amplification factor decrease with the increase in the expansion ratio at the split line. Lavery [2] accomplished the cold-flow and hot-fire experiments of a Flex-X flexible nozzle. The effects of the joint location, swing centre, expansion ratio, and swing angle are systematically analyzed. The findings were that the increase in the swing angle can result in the downstream movement of the shock wave and a decrease in the amplification factor. Strome [3] used the six-component balance to measure the aerodynamic forces of the

supersonic splitline nozzle. Yezzi et al. [4] installed the C-C materials on the throat surface and did hot-fire experiments on the supersonic splitline nozzle. The results showed that the maximum amplification factor of 1.35 can be reached with a swing angle of $5°$. Crapiz [5] compared four hot-fire experiments of the supersonic splitline nozzle, where the increase in the vector efficiency at a small swing angle can be obtained with the decrease in the expansion ratio at the splitline. Ellis et al. [6] found that the supersonic splitline nozzle increases the impulse and the amplification factor obviously, and reduces the negative mass of the engine, in contrast with the submerged vectored nozzle. Orbekk et al. [7] calculated the flowfields of the supersonic splitline nozzle based on an in-house CFD code and made some optimization of the nozzle configuration. It was found that the flow deflection is affected by the local Mach number and the upstream shock strength, and the amplification factor is mainly determined by the expansion ratio at the split line and the nozzle expansion ratio. Larrieu et al. [8] also conducted the cold-flow and hot-fire tests of the supersonic splitline nozzle. The convex and concave spheres in the joint of the nozzle model are, respectively, made up of complex materials of steel and phenolic aldehyde and alloy materials. During the tests, the amplification factor was always larger than 1.

Based on the above status, the paper focuses on the parametric study of the performance of the supersonic split line nozzle concerning the effects of the swing angle, which may give preliminary guidance on the amplification of the lateral force.

2. Numerical method

In order to capture the locations of shock waves and separation bubbles precisely, the AUSM scheme along with the third-order MUSCL interpolation method is utilized to solve the inviscid convection terms, and the k-omega SST turbulence model is adopted to simulate the interaction between the shock waves and boundary layers. The turbulent kinetic energy and dissipation term are discretized by the second-order upwind scheme, and the time integration is based on the second-order implicit iteration method. The continuity equation of fluid is written as follows

$$\frac{\partial \rho}{\partial t} + \nabla \cdot (\rho \vec{u}) = 0 \tag{1}$$

The momentum equation of fluid is expressed by

$$\frac{\partial (\rho \vec{u})}{\partial t} + \nabla \cdot (\rho \vec{u}\vec{u}) = -\nabla p - \nabla \left(\frac{2}{3}\rho k\right) + \nabla \cdot \sigma + \overrightarrow{F_d} + \rho \vec{g} \tag{2}$$

where p, $\overrightarrow{F_d}$, $\vec{g}$, and σ, respectively, denote the gas pressure, momentum source term generated by the reacting force of the solid phase, body force, and viscous stress tensor. The energy equation of fluid is written by

$$\frac{\partial (\rho e)}{\partial t} + \nabla \cdot [(\rho e + p)\vec{u}] = \nabla \cdot \left(k_{eff} \nabla T - \sum h_i \vec{J}_i + \vec{\tau} \cdot \vec{u}\right) + Q_3 \tag{3}$$

where e, $\vec{J}$, and Q_3 represent the internal energy per unit mass, diffusion vector, and energy source term caused by the small particles, respectively.

In order to track the particle trajectories accurately, the Euler-Lagrangian method along with the discrete droplet model is utilized. Regarding the small particles as discrete mass points, the motion equation of the small particles can be calculated by

$$\frac{d\vec{V}_p}{dt} = F_D\left(\vec{u} - \vec{V}_p\right) + \frac{\vec{g}(\rho_p - \rho)}{\rho_p} + \vec{F}_p \tag{4}$$

where $\vec{F}_p$, $\vec{V}_p$, and ρ_p are the additional force exerted on the particle, particle velocity, and particle density. The trajectories of the small particles are determined by

$$\frac{\partial \vec{r}_p}{\partial t} = \vec{V}_p \tag{5}$$

The energy equation of the small particles is expressed by

$$m_p C_p \frac{dT}{dt} = h_p A_p \left(T - T_p\right) \tag{6}$$

where h_p and A_p are the surface convective heat transfer coefficient and surface area. In the Lagrangian frame, every particle should be traced, and the exchanged parameters between the solid and fluid phases are iterated till numerical convergence. The distribution of small particles follows the Rosin-

Rammler law, and the nozzle inlet and exit are set to the escape boundary conditions for particles. In addition, the grid size should ensure that y+ is close to 1.

3. Numerical verification

In order to demonstrate the reliability of the present numerical scheme on the gas-particle nozzle flowfield, the planar nozzle experiment conducted by Okuda et al. [9] is adopted. As shown in Fig.3, the contraction and expansion ratios of the selected nozzle configuration are, respectively, 4.4 and 4.0, and the lengths of the converging and diverging sections are 0.02 and 0.1 m. The length of the constant-area channel installed at the exit of the diverging section is 0.03 m. The total pressure and temperature at the nozzle inlet are 392 kPa and 293 K, respectively, and the ambient pressure is low enough to avoid shock waves in the nozzle. The grids near the walls and throat are densely clustered to satisfy the requirement of y+ = 30 ~ 60. Because the injected particles in this experiment are not close to the melting state and are non-sticky, the wall boundary for the discrete phase is set to the complete reflection condition. As for solid rocket nozzles, the wall boundary condition should be converted into the trap condition.

Moreover, the material of injected particles for the numerical verification is polystyrene with a density of 1.05 g·cm-3 and calibrated particle diameters of 545 and 1095 μm, and the particle injection velocity is set to 20 m·s-1. Although the particle material is not aluminum trioxide, the numerical verification still implies the feasibility of the core algorithm in similar application scenarios. As displayed in Fig.4, most particles with two different particle diameters are concentrated along the middle line of the nozzle diverging section, and only a few particles wander near the nozzle walls. The particle velocities along the nozzle middle line in the simulation and experiment match well (see Figure 5), revealing that the present numerical method is reliable in simulating the gas-particle flow.

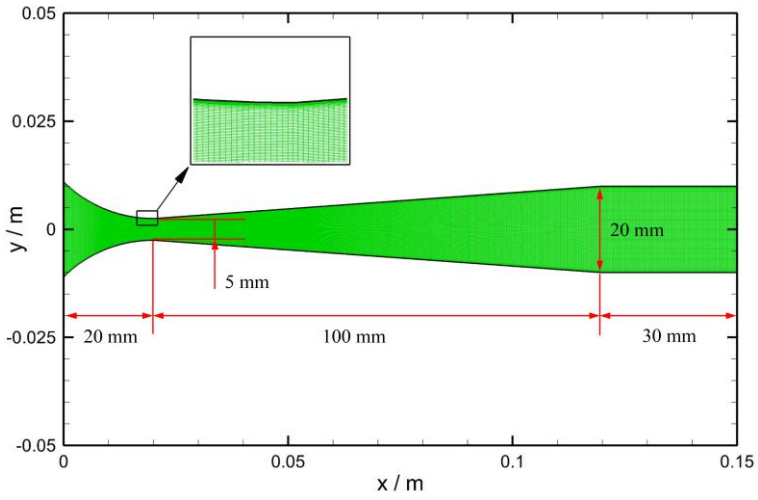

Fig 3. Grids and configuration of a planar gas-particle nozzle

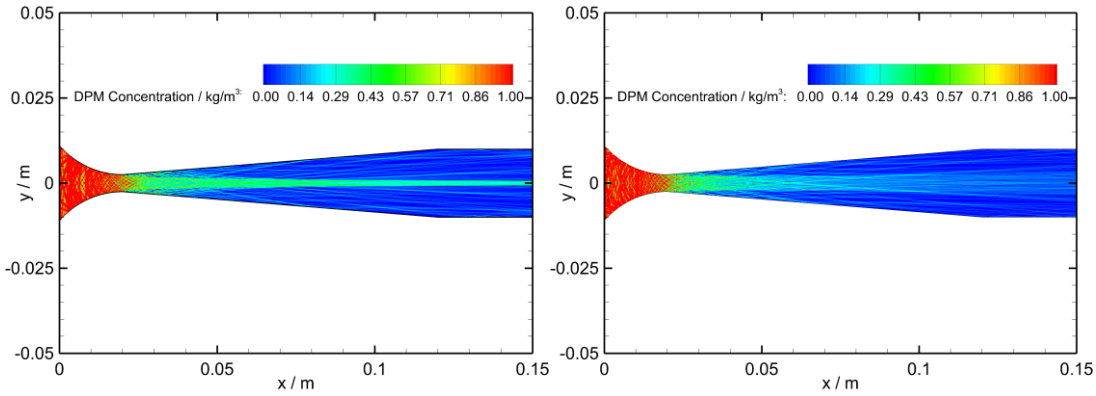

(a) d_p = 545 μm (b) d_p = 1095 μm

Fig.4 Discrete phase concentrations of different particle diameters in the nozzle

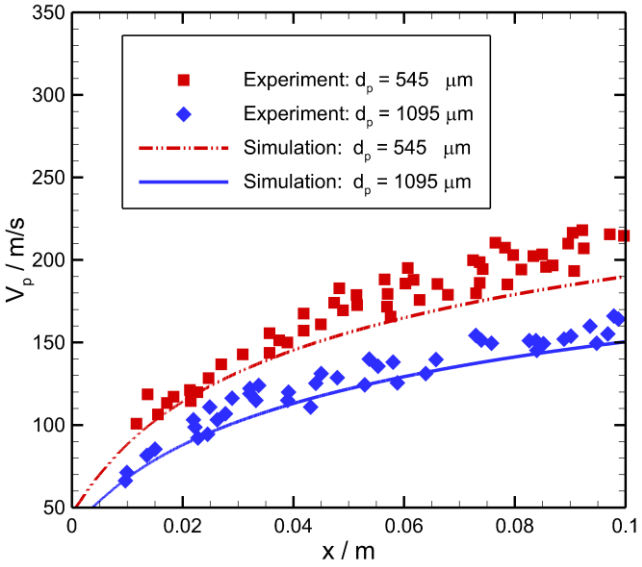

Fig.5 Particle velocity as a function of the distance from the nozzle throat

4. Discussion

In order to illustrate the influence of the initial arc radius on the aerodynamic performance, the nozzle flowfields for initial arc radii of 0, 5, 10, and 15 mm are simulated. The flow parameters of boundaries in the computational domain are consistent with the values mentioned in Section 2.3. As depicted in Figs.6 (a) and (b), a nozzle without an initial arc radius contains central expansion fans emitted from the throat cusps, which abruptly changes the flow speed and deflection angle. Without the swing of the nozzle skirt, two internal shock waves are in symmetrical formation, and their intersection point is close to the nozzle exit. With a swing angle of 6°, the internal shock wave from the lower throat cusp disappears, and the strength of the shock wave at the forward-facing step is relatively weak. Meanwhile, the trailing shock wave at the backward-facing step decelerates the flow from M = 2.45 to M = 2.19, and the low-speed zone in front of the forward-facing step extends upstream to the throat. As shown in Figs.6 (c) and (d), a nozzle with an initial arc radius of 15 mm scatters the expansion waves, and the Mach isolines near the axis are distorted significantly. Without the swing of the nozzle skirt, no apparent internal shock waves exist. With a swing angle of 6°, the low-speed zone is concentrated near the forward-facing step and forms an imaginary wedge that induces a shock wave. This shock wave is then bent by the central expansion fan emitted from the edge of the forward-facing step and extends to the nozzle exit. In addition, there is no intersection point of shock waves in the nozzle diverging section.

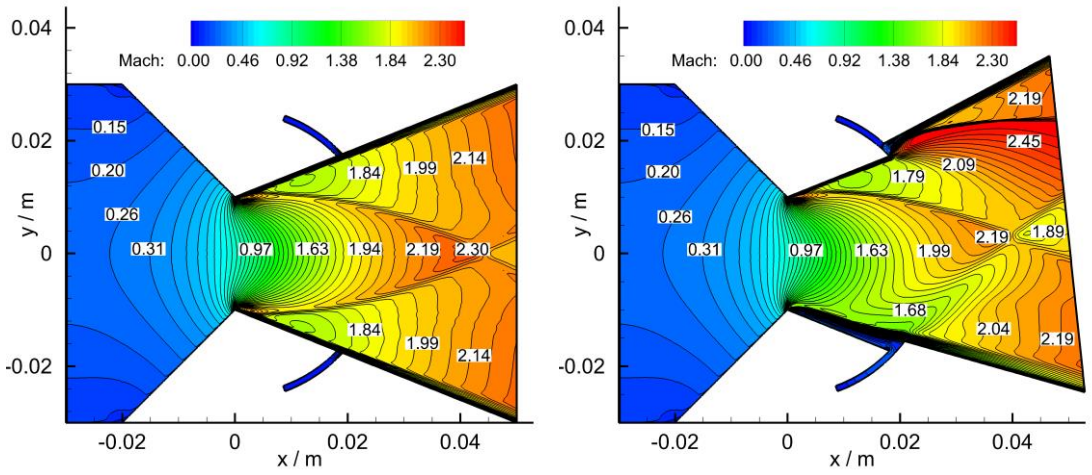

(a) r_i = 0 mm, θ = 0°

(b) r_i = 0 mm, θ = 6°

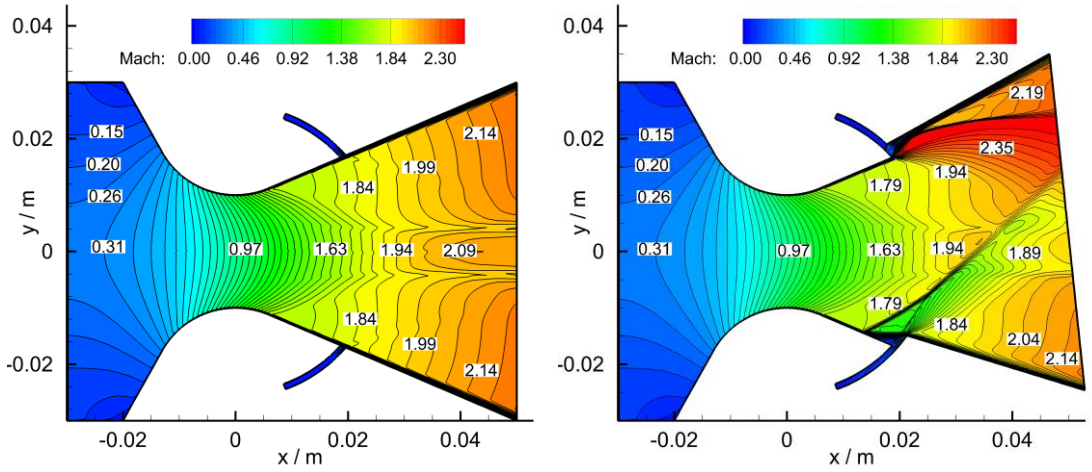

(c) r_i = 15 mm, θ = 0° (d) r_i = 15 mm, θ = 6°

Fig.6 Gas-phase Mach number contours of nozzles with different initial arc radii at two typical swing angles

As plotted in Fig.7, the trajectories of heavy particles are closer to the axis, and light particles seem to be easier to approach the nozzle wall. However, due to the effects of the aerodynamic drag and particle inertia, there are limiting particle streamlines, which isolate the particle-free and two-phase regions. Combined with the conditions in Fig.6, the central expansion fan emitted from the cuspidal point of the throat can broaden the trajectory boundary width of the heavy particles, and the scattered expansion waves caused by the large initial arc radius have little effect on the movements of heavy particles. For a swing angle of 6°, the asymmetric distributions of heavy particles are suppressed with the increase in the initial arc radius, and the trajectory envelopes of light particles in the nozzle diverging section can always be adapted to the flow conditions.

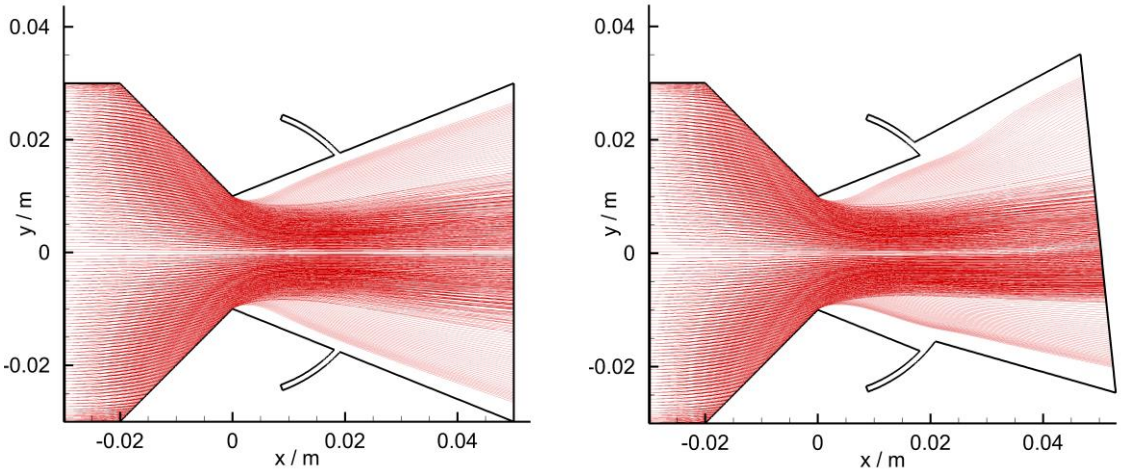

(a) r_i = 0 mm, θ = 0° (b) r_i = 0 mm, θ = 6°

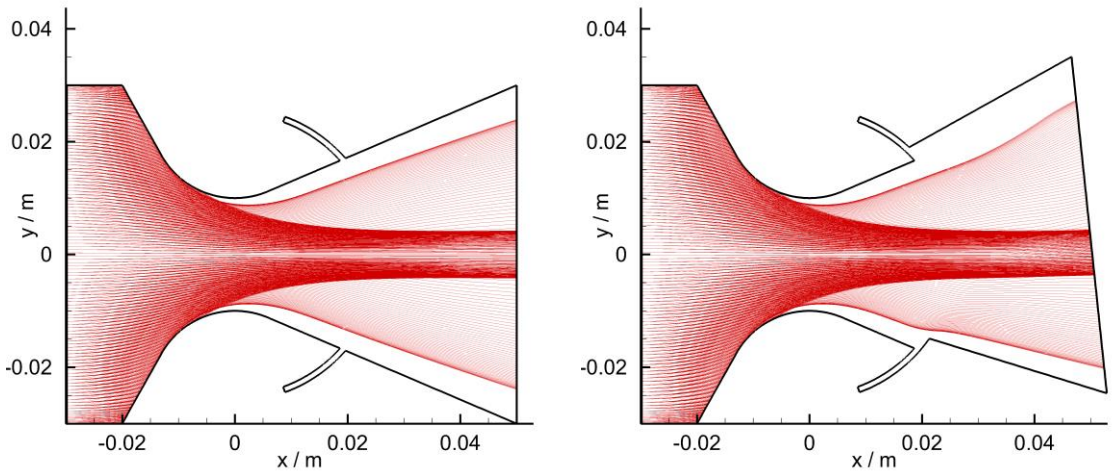

(c) r_i = 15 mm, θ = 0° (d) r_i = 15 mm, θ = 6°

Fig.6 Discrete particle trajectories in the nozzles with different initial arc radii at two swing angles

As displayed in Fig.7, slight drops in the thrust coefficients are generally observed with the increase in the swing angle of the nozzle skirt. Most of the thrust coefficients with initial arc radii are above 0.92, and their maximum values are obtained at θ = 0 and can reach 0.944 ~ 0.952. Meanwhile, those without an initial arc radius are in the range of 0.896 ~ 0.912. With the swing angle below 2°, the thrust coefficients with initial arc radii of 10 and 15 mm almost coincide. When the swing angle exceeds 4°, the deviations of thrust coefficients between the initial arc radii of 10 and 15 mm are enlarged.

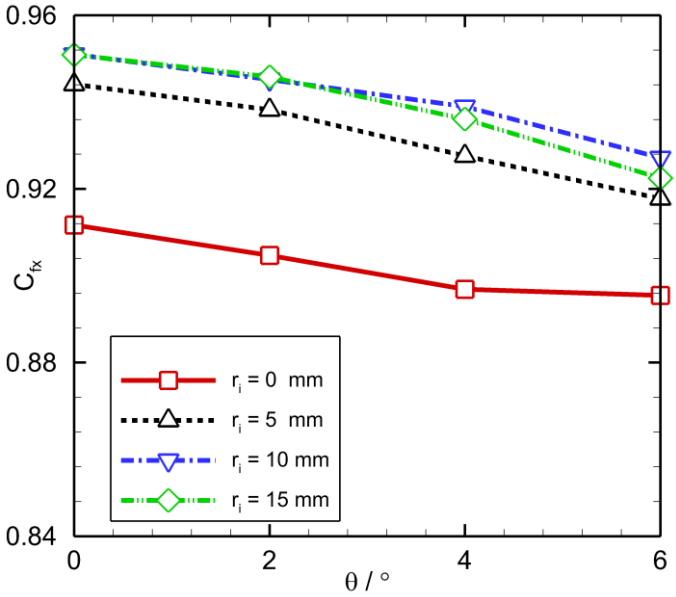

Fig.7 Influence of the initial expansion radius on the axial thrust coefficient

As exhibited in Fig.8 (a), the amplification factor that denotes the ratio of the thrust vector angle to the mechanical swing angle for the case with an initial arc radius of 10 mm always keeps above 1.29, and those for the cases with initial arc radii of 5 and 15 mm are below 1.27 at the swing angle of 4°. The maximum variations of the amplification factors for the cases with initial arc radii of 0, 5, 10, and 15 mm at non-zero swing angles are, respectively, 0.108, 0.031, 0.049, and 0.521. As described in Fig.8 (b), the thrust vector angles have an approximately linear relation with swing angles, of which the slopes are almost identical. With the swing angle of 6°, the thrust vector angle reaches 7.3° ~ 7.8°. It can be found that the initial arc radius controls the aggregations of the expansion waves, thereby affecting the pressure decaying process near the nozzle throat and changing the aerodynamic performance. The initial arc radius is then set to 10 mm for the following optimization, thus preliminarily balancing the axial thrust and the amplification of the lateral force.

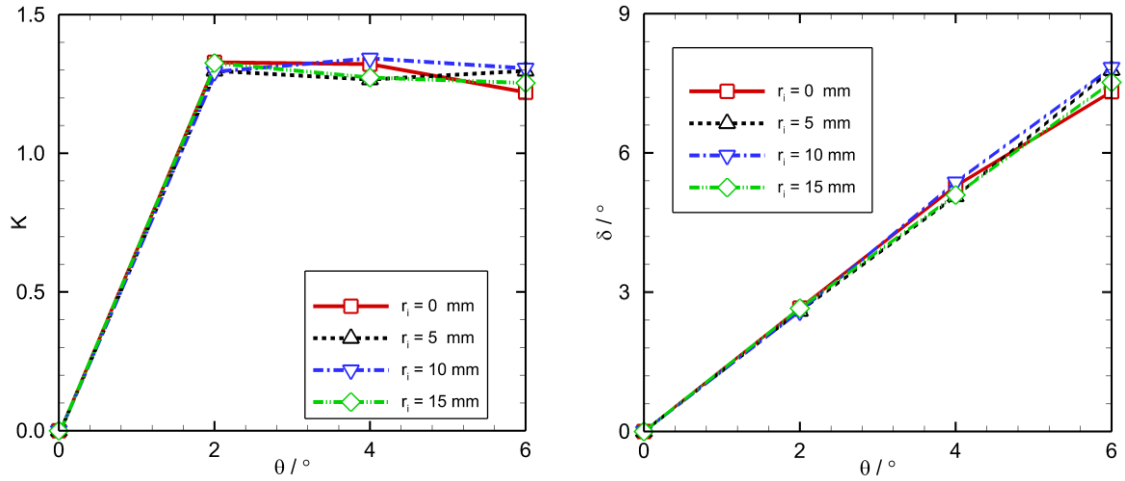

(a) Amplification factor (b) Thrust vector angle

Fig.8 Influence of the initial arc radius on the amplification factor and thrust vector angle

On the premise that the length of the nozzle diverging section aforementioned is utilized as a reference length, the cases with length ratios L/L0 = 1/2, 1/1, 3/2, and 2/1 are successively simulated to reveal the effects on aerodynamic performance. As displayed in Fig.9, the included angle between two nozzle diverging walls decreases with the increase in the length of the nozzle diverging section. With L/L0 = 1/2, a large part of the flow is not parallel to the axis, and the splitline is close to the nozzle exit. When the short nozzle skirt swings to 6°, the forward-facing step induces a shock wave almost parallel to the horizontal direction, and only central expansion fans are emitted from the edge of the backward-facing step. With L/L0 = 2/1, the flow acceleration is more moderate, and the exit Mach number never exceeds 2.30. It can also be noticed that the Mach numbers at the axis are lower than the Mach numbers on its two sides, partially implying the energy dissipation caused by the particle drag. When the long nozzle skirt swings to 6°, the shock wave generated by the forward-facing step impinges on the opposite wall, and its reflected shock wave merges with the trailing shock wave.

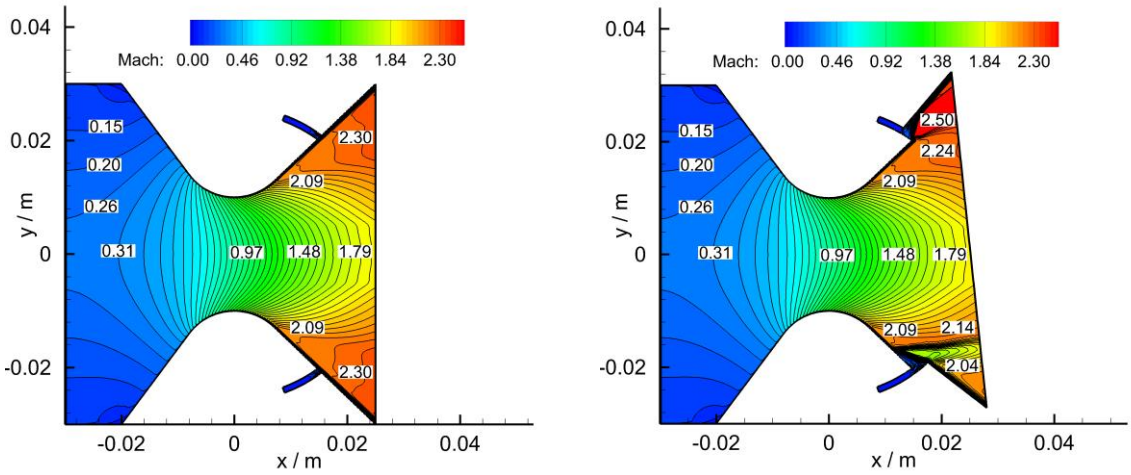

(a) L/L_0 = 1/2, θ = 0° (b) L/L_0 = 1/2, θ = 6°

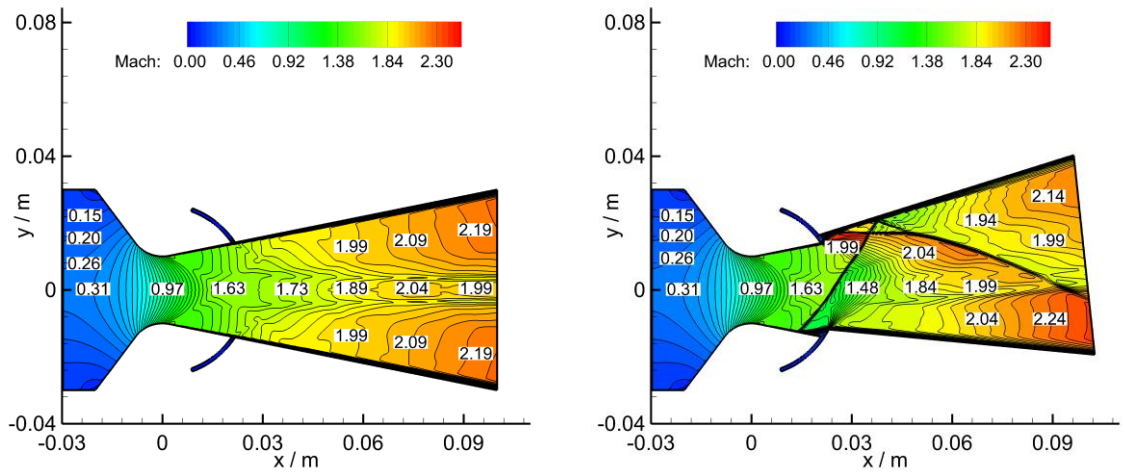

(c) L/L_0 = 2/1, θ = 0° (d) L/L_0 = 2/1, θ = 6°

Fig.9 Gas-phase Mach number contours of nozzles with different nozzle lengths at two typical swing angles

As illustrated in Fig.10, the space distributions of heavy and light particles are pretty similar to the descriptions aforementioned, and the trajectories of light particles are still sensitive to the flowfields. Moreover, the upward bending of their trajectory envelope reveals the cumulative effects of aerodynamic forces on the heavy particles in a long nozzle diverging section. For the cases with non-zero initial arc radii and different lengths of nozzle diverging sections, the detachment points of the particle trajectories from the wall are all located at the nozzle converging section, and the swing of the nozzle skirt usually drives the light particles to distribute more in the rotating direction. However, an exception with L/L0 = 1/2 and θ = 6° still exists, where more than half of light particles distribute in the opposite rotating direction. The corresponding reason is that the particle inertia can overcome the aerodynamic drag due to the short interaction time in a short nozzle diverging section, and the asymmetric configuration after the swing of the nozzle skirt elongates the nozzle length of the lower side, allowing a little more flow expansion in the axial direction.

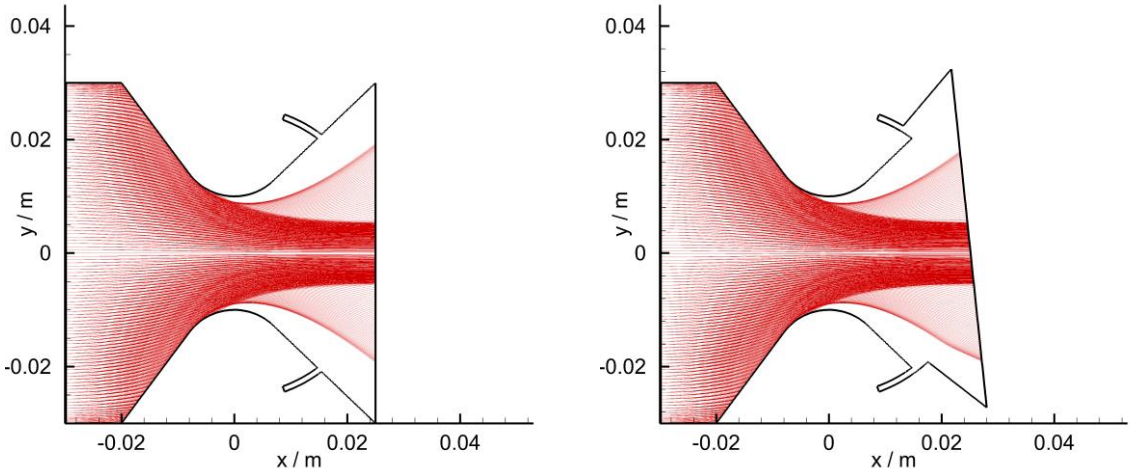

(a) L/L_0 = 1/2, θ = 0° (b) L/L_0 = 1/2, θ = 6°

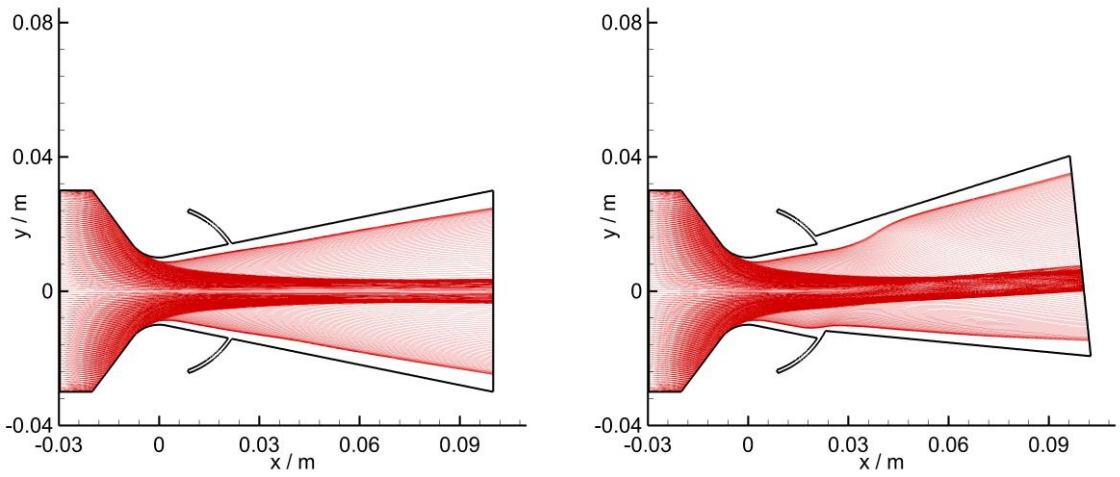

(c) L/L_0 = 2/1, θ = 0° (d) L/L_0 = 2/1, θ = 6°

Fig.10 Discrete particle trajectories of nozzles with different nozzle lengths at two typical swing angles

As described in Fig.11, the continuous increase in the thrust coefficient is noticed with the increase in the length of the nozzle diverging section, implying that the axial guidance of the long nozzle diverging section is beneficial for smooth and moderate flow acceleration. For the case with L/L0 = 1/2, the thrust coefficient fluctuates around 0.87. When L/L0 exceeds 1/1, the growth rate of the thrust coefficient concerning the length of the nozzle diverging section slows down, but their absolute values remain above 0.92. With the swing angle changing from 0 to 6°, the thrust coefficients for L/L0 = 1/1, 3/2, and 2/1 only drop by 2.51%, 1.46%, and 1.75%, respectively.

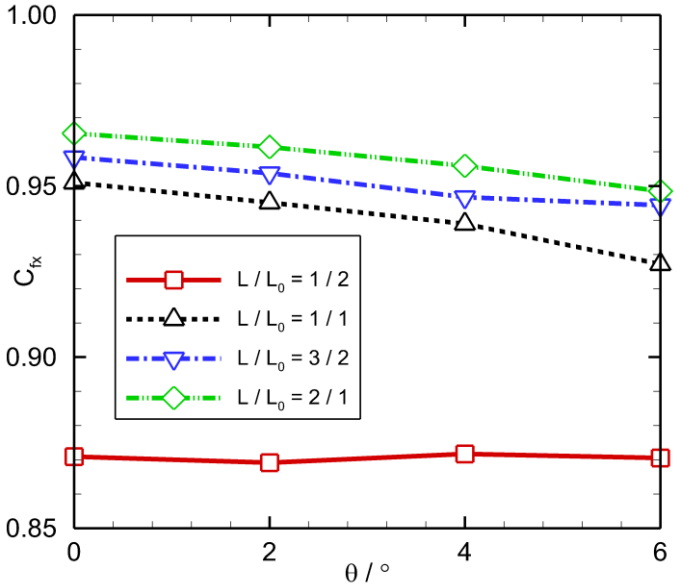

Fig.11 Influence of the nozzle length on the axial thrust coefficient

As depicted in Fig.12 (a), the amplification factor first increases and then drops with the length of the nozzle diverging section changing from L/L0 = 1/2 to L/L0 = 2/1 at the non-zero swing angles. For the cases with L/L0 = 1/2, 1/1, and 2/1, the amplification factor at non-zero swing angles, respectively, fluctuates around 0.62, 1.31, and 1.05. As for the case with L/L0 = 3/2, the amplification factor drops by 17.02% with the increase in the swing angle from 2° to 6°. As shown in Fig.12 (b), the cases with L/L0 = 1/1 and 2/1 exhibit more linear relations between the swing angle and the thrust vector angle, but the growth rates of the thrust vector angle for cases with L/L0 = 1/2 and 3/2 gradually decrease. The maximum thrust vector angles of L/L0 = 1/2, 1/1, 3/2, and 2/1 are, respectively, 3.58°, 7.84°, 7.00°, and 6.38° at the swing angle of 6°. It can be observed that the length of the nozzle diverging section tightly controls the downstream topology evolution of the expansion waves and shock waves. When the shock wave generated by the forward-facing step reflects on the opposite wall, the pressure

difference between two diverging nozzle walls is reduced, decreasing the lateral force. When the diverging nozzle walls are too short, their horizontal projection areas are reduced, reducing the lateral force as well. Consequently, the nozzle with ri = 10 mm and L/L0 = 1/1 is chosen as the baseline configuration for the following parametric studies of the diverging section profile and the swing center.

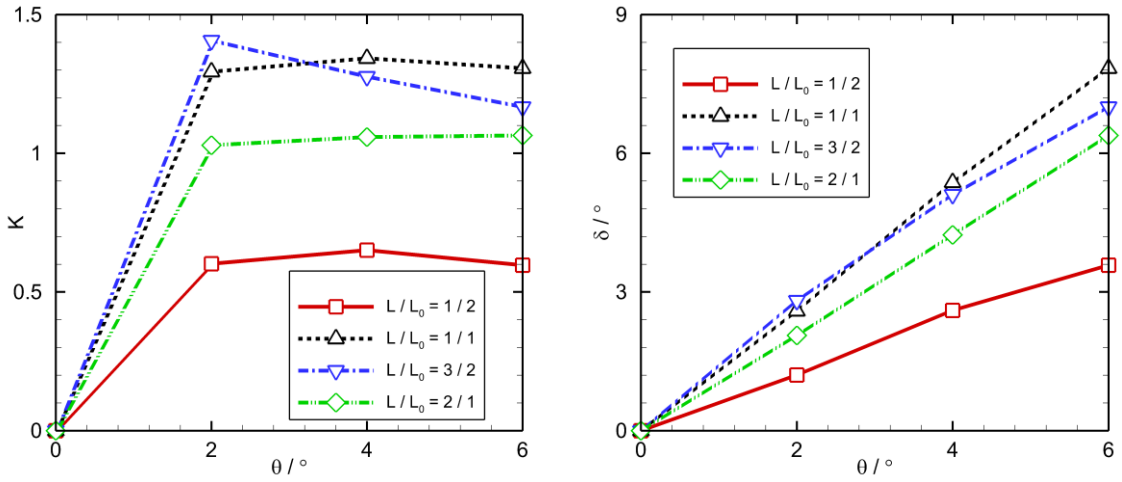

(a) Amplification factor (b) Thrust vector angle

Fig.12 Influence of the nozzle length on the amplification factor and thrust vector angle

Given that the initial arc radius and the length of the nozzle diverging section have been optimized, the thrust boosting can be further achieved by profile modifications of diverging sections. Conventionally, the nozzle diverging profiles can be represented by a Bezier curve that contains a series of control points and is optimized by the simplex method or machine learning technique. However, it sometimes may result in the expansion of search space. For the convenience of model design, the transition curves are directly set to large secondary circular arcs tangential to the initial arc, of which the terminal points at the nozzle exit are kept at x = 0.05 m without the swing of the nozzle skirt. Due to location differences of circle centers for the transition curves, the nozzle diverging sections have concave and convex configurations. As shown in Fig.13, the Mach numbers at the nozzle exit are low in the core region and high in the transition region for the concave configurations, but the trends for the convex configurations are reversed. At the exit of the concave configuration with rs = 100 mm and θ = 0, the core Mach number is 1.89, and the Mach number in the transition region is 2.19. At the exit of the convex configuration with rs = 100 mm and θ = 0, the core Mach number reaches 2.24, and the Mach number in the transition region drops to 2.04. With the swing angle of 6°, the shock wave emitted from the forward-facing step intersects with the trailing shock wave behind the backward-facing step for the concave nozzle configuration, and no intersection points of shock waves are found in the convex nozzle configuration. In addition, the starting points of the shock wave on the lower side for the convex nozzle configurations are more upstream than the concave ones.

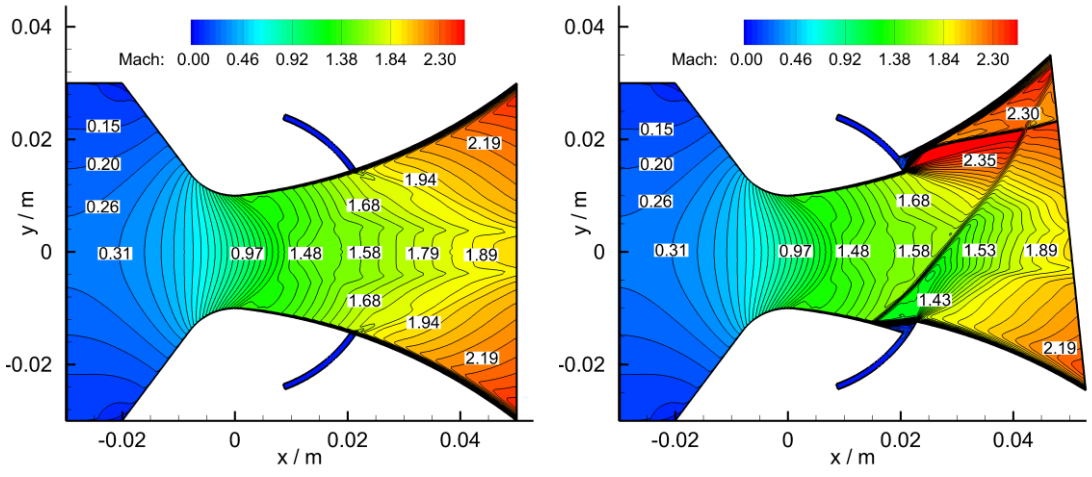

(a) Concave, r_s = 100 mm, θ = 0° (b) Concave, r_s = 100 mm, θ = 6°

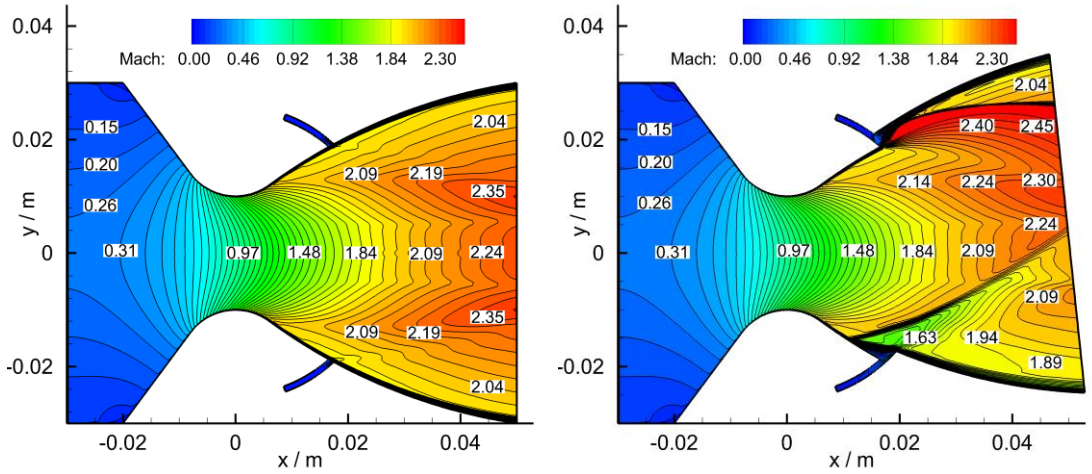

(c) Convex, r_s = 100 mm, θ = 0° (d) Convex, r_s = 100 mm, θ = 6°

Fig.13 Mach contours of nozzles with different diverging section profiles at two typical swing angles

As plotted in Fig.14, the transition of the nozzle diverging section from a concave shape to a convex shape broadens the width of the trajectory envelope for heavy particles, and the free-particle regions occupy a shorter height at the nozzle exit. Meanwhile, the density of heavy particles near the axis gradually increases for the concave configuration, while those for the convex configuration first increase and then decrease from upstream to downstream.

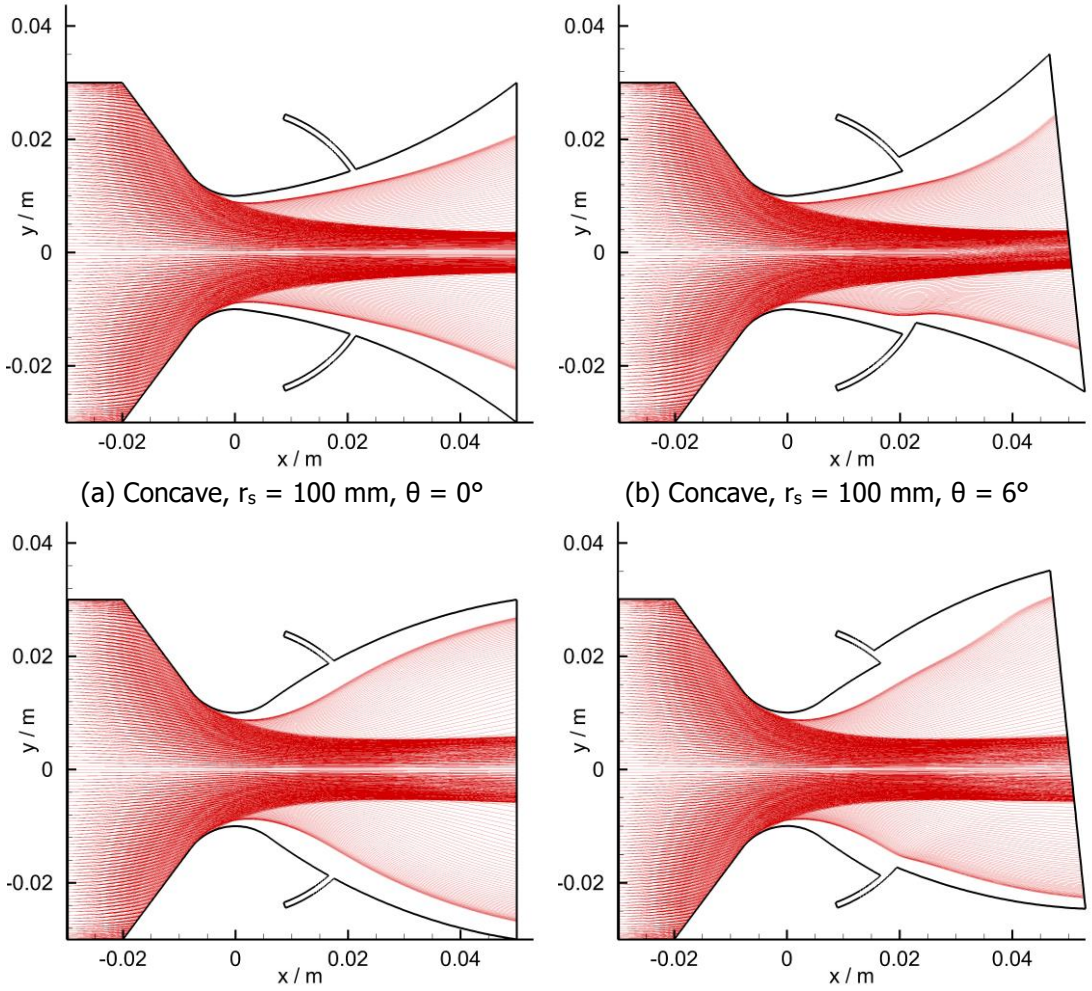

(a) Concave, r_s = 100 mm, θ = 0° (b) Concave, r_s = 100 mm, θ = 6°

(c) Convex, r_s = 100 mm, θ = 0° (d) Convex, r_s = 100 mm, θ = 6°

Fig.14 Discrete particle trajectories of nozzles with different diverging section profiles at two typical swing angles

As shown in Fig.15, the thrust coefficient increases dramatically with the decrease in the inward bending degrees of nozzle diverging walls. However, the outward bending of nozzle diverging walls only brings limited changes to the thrust coefficient. In contrast with the concave configuration of rs = 100 mm, the relative increments of thrust coefficient for the straight nozzle diverging section are, respectively, 2.83%, 3.01%, 3.58%, and 3.88% at the swing angles of 0°, 2°, 4°, and 6°. For the convex configuration of rs = 100 mm, its thrust coefficient almost coincides with the straight nozzle diverging section at the swing angles of 0, 2°, and 4°, and is higher than the other four nozzle diverging profiles at the swing angle of 6°. As for the convex configuration of rs = 200 mm, the maximum thrust coefficient of 0.9543 is obtained without the swing of the nozzle skirt, and it drops by 1.96% with the increase in the swing angle.

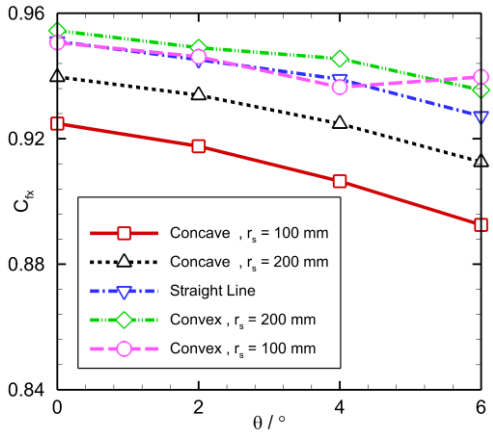

Fig.15 Influence of the diverging section profile on the axial thrust coefficient

As illustrated in Fig.16 (a), the amplification factor is only influenced when the inward or outward bending of the nozzle diverging wall exceeds certain levels. When the radius of the transition region is large enough (rs = 200 mm), the amplification factor fluctuates around 1.30 at non-zero swing angles and is close to the straight wall condition regardless of the bending direction of the nozzle diverging section. When the radius of the transition region is relatively small (rs = 100 mm), the inward and outward bending of the nozzle diverging section, respectively, bring the decrease and increase in the initial expansion angle, modifying the pre-shock conditions at the forward- and backward-facing steps. The amplification factors of the concave and convex configurations with rs = 100 mm are approximately situated at 1.40 and 1.25, respectively, at non-zero swing angles. As depicted in Fig.16 (b), all the nozzle diverging profiles precisely follow the linear relations between the swing and thrust vector angles. Once the swing angle exceeds 2°, the discrepancies of thrust vector angles are enlarged. When the swing angle reaches 6°, the thrust vector angle obtained by the convex configuration with rs = 100 mm exceeds the concave one with the same secondary radius by 11.42%.

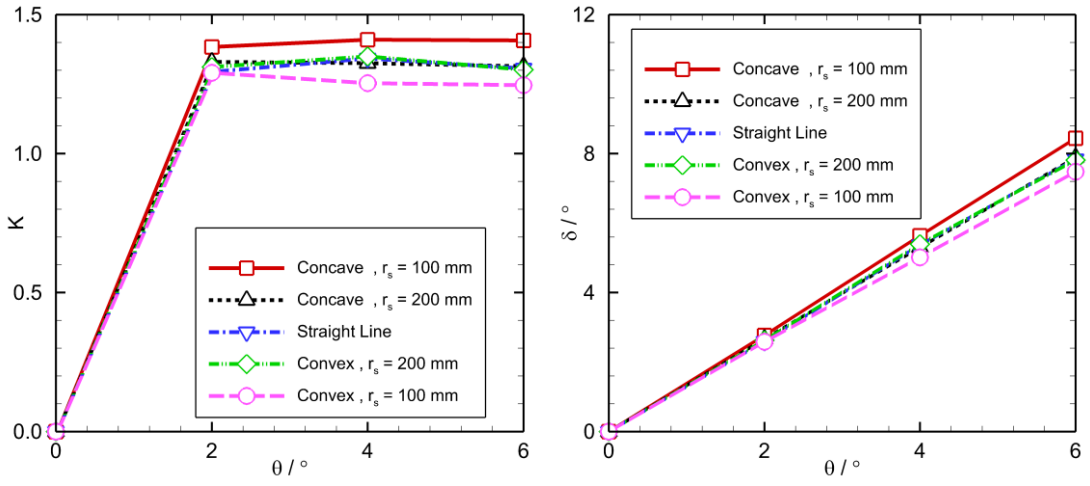

(a) Amplification factor (b) Thrust vector angle

Fig.16 Influence of the diverging profile on the amplification factor and thrust vector angle

The axial location of the swing center determines the scale of the nozzle skirt, thus changing the location of the splitline on the nozzle diverging wall. Five nozzles with different locations of swing center (xc = -10, -5, 0, +5, and +10 mm) are numerically investigated to describe the changing trends of aerodynamic performance. As shown in Fig.17, the splitline creates a segment of aerodynamic boundary that bridges the upstream and downstream nozzle walls. When the splitline gets close to the throat, the thin boundary layer is more sensitive to the wall discontinuity, generating weak compression waves that slow down the core region. When the splitline is placed in the middle of the nozzle diverging section, the thick boundary layer can dampen the wall disturbances. With the swing angle of 6°, the shock wave induced by the forward-facing step and the trailing shock wave behind the backward-facing step appear and move downstream synchronously with the splitline.

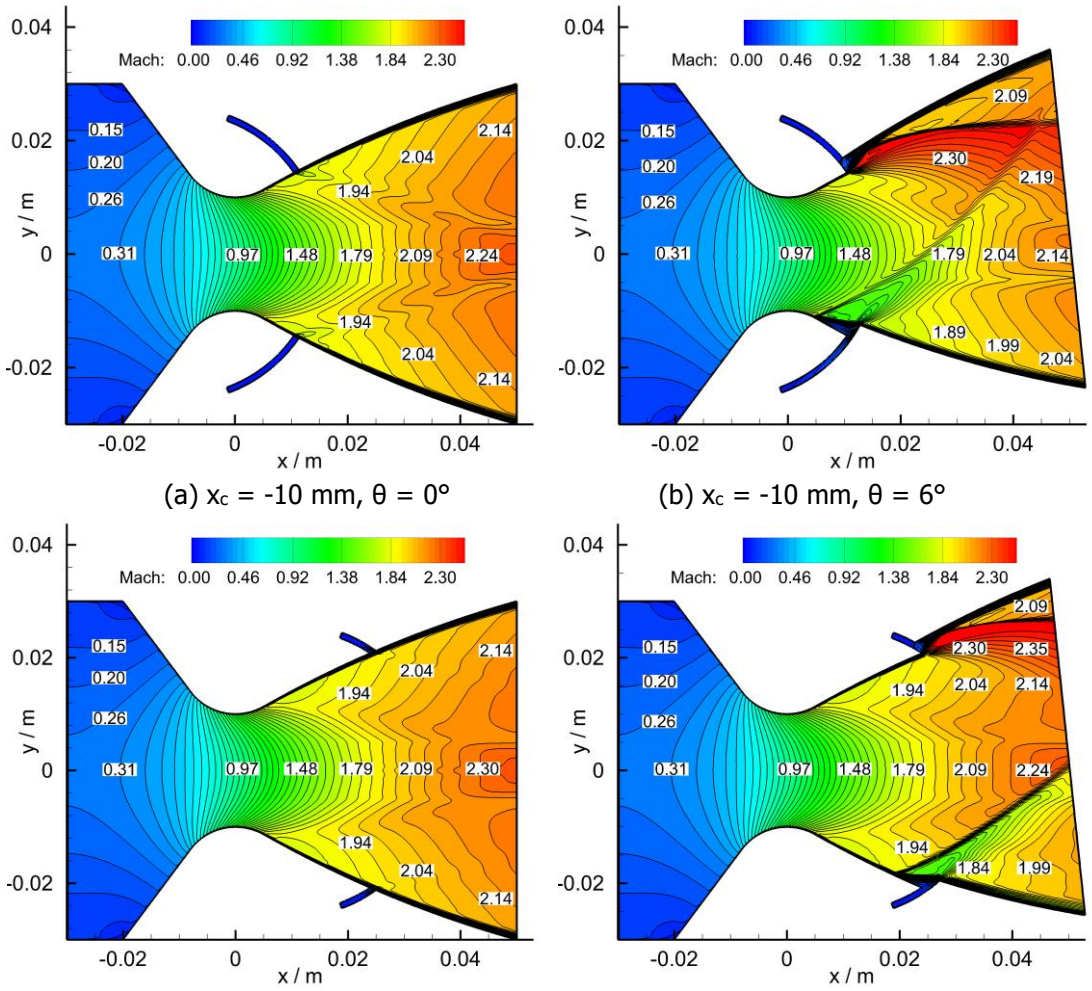

(a) x_c = -10 mm, θ = 0° (b) x_c = -10 mm, θ = 6°

(c) x_c = +10 mm, θ = 0° (d) x_c = -10 mm, θ = 6°

Fig.17 Gas-phase Mach number contours of nozzles with different swing centers at two typical swing angles

As described in Fig.18, the minor differences in flowfields caused by the locations of splitlines are insufficient to change the particle distributions without the swing of the nozzle skirt. The effective way to divert the particle trajectories is still the intrusion of the wall discontinuity at non-zero swing angles. With the downstream movements of splitlines, the asymmetric particle distribution gradually crumbles. For the case with xc = -10 mm and θ = 6°, a portion of heavy particles at the nozzle exit roll up. For the case with xc = +10 mm and θ = 6°, the motion directions of the heavy particles are almost symmetric to the axis.

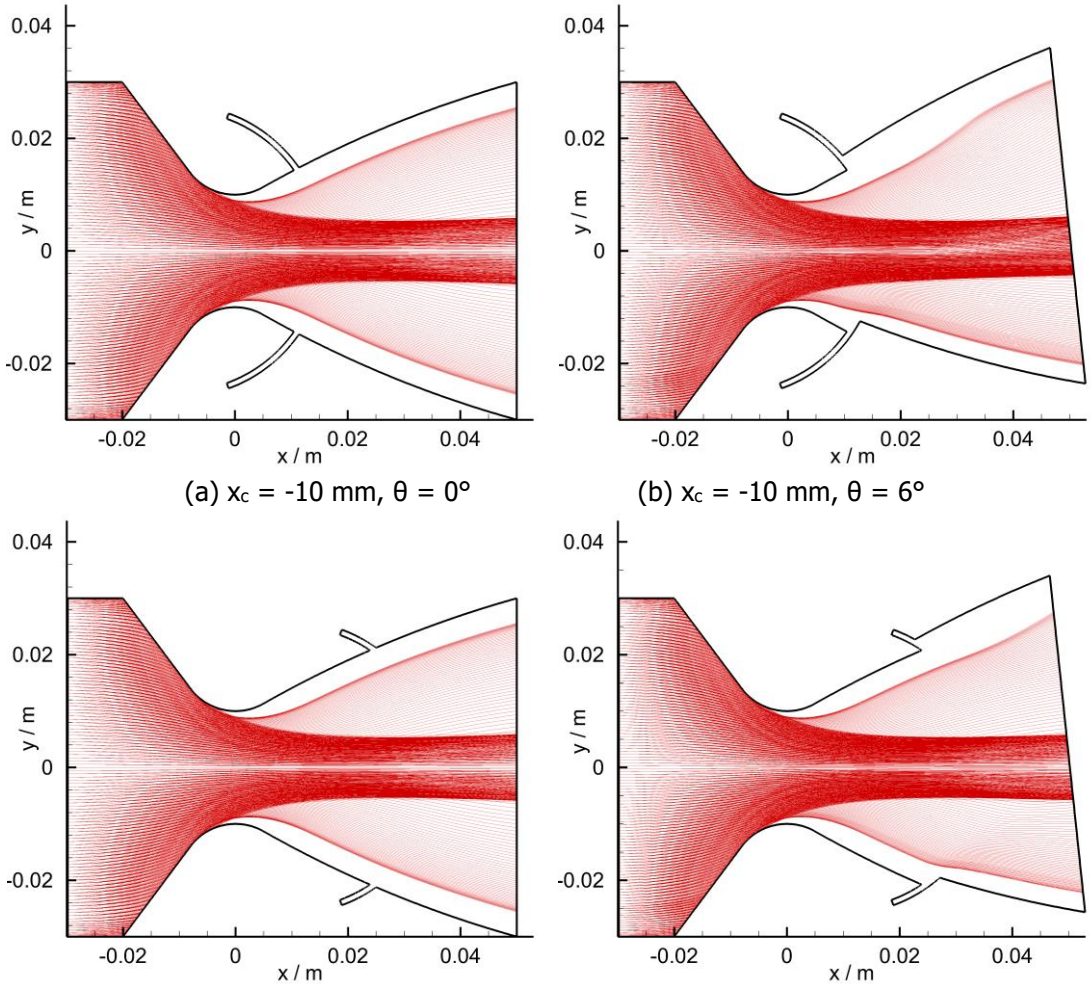

(a) x_c = -10 mm, θ = 0° (b) x_c = -10 mm, θ = 6°

(c) x_c = +10 mm, θ = 0° (d) x_c = +10 mm, θ = 6°

Fig.18 Discrete particle trajectories of nozzles with different swing centers at two typical swing angles

As displayed in Fig.19, the swing centers downstream of the nozzle throat are not responsible for the mutation of the thrust coefficient. For the swing centers at xc = 0, +5, and +10 mm, all the thrust coefficients roughly drop by 1.89% with the increase in the swing angle from 0° to 6°. For the swing centers at xc = -5 and -10 mm, the thrust coefficients at the swing angle of 2° are lower than those at 4°. With a convex nozzle diverging section, the abnormal drop in thrust coefficient is that bow shock waves form in front of the forward-facing step at a small swing angle while oblique shock waves are induced by an imaginary wedge of recirculation zone.

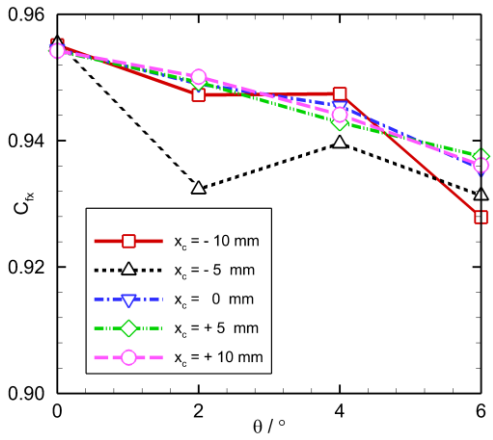

Fig.19 Influence of the swing center on the axial thrust coefficient

As shown in Fig.20 (a), the amplification factor decreases with the downstream movement of the swing center at non-zero swing angles. For the swing centers at xc = +5 and +10 mm, the amplification factors, respectively, keep at 1.186 and 1.082. For the swing centers at xc = 0 and -5 mm, the amplification factors slightly fluctuate around 1.350. With the swing angle of 4°, the maximum amplification factor of 1.541 is obtained at xc = -10 mm. As exhibited in Fig.20 (b), the cases with xc = +5 and +10 mm follow the linear relation between the thrust vector angle and swing angle, but the thrust vector angles in the cases with xc = -10, -5, and 0 mm change nonlinearly. The average slope of the thrust vector angle to the swing angle increases with the upstream movement of the swing center, except that the conditions of xc = -5 and 0 mm are adjacent. With the swing angle of 6°, the corresponding thrust vector angles for xc = -10, -5, 0, +5, and +10 mm reach 8.48°, 8.28°, 7.76°, 7.02°, and 6.44°, respectively.

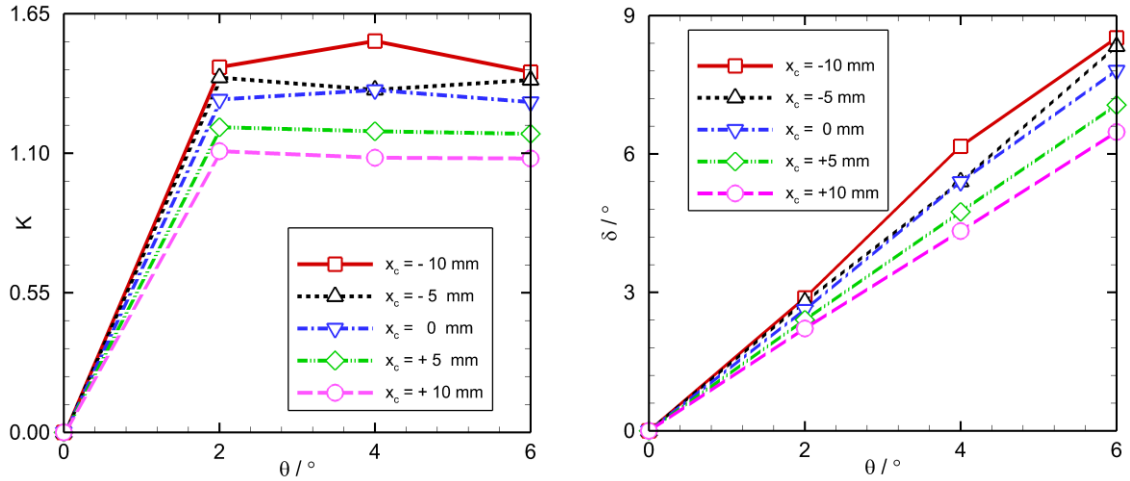

(a) Amplification factor (b) Thrust vector angle

Fig.20 Influence of the swing center on the amplification factor and thrust vector angle

5. Conclusion

This study investigates the optimal aerodynamic configuration of SSSL nozzles with two-phase interactions and related effects of the swing angular velocity on the dynamic responses. The performance sensitivities of the initial arc radius, diverging section length, diverging section profile, and swing center location are parametrically studied. The conclusions are listed as follows:

(1) The increase in the initial arc radius decelerates the pressure decaying process along the nozzle diverging walls, thus raising the force caused by the pressure difference. Meanwhile, the existence of the initial arc radius concentrates heavy particles along the axis and scatters light particles to the nozzle transition region. When the initial arc radius is selected to 10 mm, the amplification factor and the maximum thrust vector angle can remain above 1.29 and reach around 7.8°, respectively.

(2) Increasing the total nozzle length complicates the nozzle flowfields with a small swing angle. When the nozzle length is too long, the shock wave induced by the forward-facing step may reflect on the opposite wall, and the amplification factor is close to one. When the nozzle length is too short, the effects of the shock waves and expansion fans on the airflow and solid particles are limited, and the amplification factor drops far below one. In addition, the slope of the thrust vector angle to the swing angle for a moderate nozzle length is larger than the other nozzle configurations.

(3) A convex diverging profile with a large secondary radius is beneficial for the balance among the thrust coefficient, amplification factor, and thrust vector angle because more flow expansion and acceleration are achieved in the middle of the nozzle flowpath instead of at the nozzle exit. With the convex arc radius of 200 mm, the maximum thrust coefficient of 0.9543 is obtained at a zero swing angle, and thrust coefficient deviations of non-zero swing angles are below 1.96%. Meanwhile, its amplification factor fluctuates around 1.30 at non-zero swing angles, and its linear relation between the swing angle and the thrust vector angle is not affected too much.

(4) When the swing center moves axially from upstream to downstream of the throat, the thrust coefficient mutation is gradually smoothed out. However, the amplification factor and the thrust vector angle are raised with the reverse movement of the swing center.

Acknowledgement

We would like to acknowledge the support of the National Science and Technology Major Project on contract number J2019-II-0007-027. We are also grateful to the editors and reviewers.

References

1. Strahle, W. C.: A theory of the aerodynamics of the supersonic splitline gimbaled nozzle. J. Spacecr. 4(2), 262-269 (1967)
2. Lavery, R.: Flexible exit cone nozzle development program phase II: Report: Volume II cold flow tests [R]. Air Force Rocket Propulsion Laboratory (1968)
3. Strome, R. K.: Test firing of a supersonic split-line nozzle [R]. Air Force Rocket Propulsion Laboratory (1969)
4. Yezzi, C. A., Gainesville, V. A.: Thrust vector control technology demonstration [R]. America Institute of Aeronautics and Astronautics (1986)
5. Crapiz, D.: Improvements in composite tactical solid rocket motor technology [R]. America Institute of Aeronautics and Astronautics (1990)
6. Ellis, R., Berdoyes, M.: Supersonic split line (SSSL) flexseal nozzle technology evaluation program [R]. America Institute of Aeronautics and Astronautics (1997)
7. Orbekk, D. E.: Supersonic split line TVC technology and testing at Nammo Raufoss AS [R]. America Institute of Aeronautics and Astronautics (2006).
8. Larrieu, J. M., Ceccarelli, A. L.: Supersonic split line cold ball & socket nozzle (SSCBSN), a cost-effective and compact thrust vector control solution for booster and cruise stages [C]//5th European Conference for Aeronautics and Space Science (2013)
9. Okuda, S., Choi, W.: Gas-particle mixture flow in various types of convergent-divergent nozzle. J. Chem. Eng. Jpn. 11(6), 432-438 (1978)

